RESEARCH PAPER

Simultaneous visualization of the flow inside and around droplets generated in microchannels

Manuela R. Duxenneuner · Peter Fischer · Erich J. Windhab · Justin J. Cooper-White

Abstract This paper reports the visualization of droplet formation in co-flowing microfluidic devices using food-grade aqueous biopolymer–surfactant solutions as the dispersed droplet phase and sunflower oil as the continuous phase. Microparticle image velocimetry and streak imaging techniques are utilized to simultaneously recover the velocity profiles both within and around the dispersed phase during droplet formation and detachment. Different breakup mechanisms are found for Newtonian–Newtonian and non-Newtonian–Newtonian model water-in-oil emulsions, emphasizing the influence of process and material parameters such as the flow rates of both phases, interfacial tension, and the elastic properties of the non-Newtonian droplet phase on the droplet formation detachment dynamics.

Keywords Microparticle image velocimetry ·
Co-flow geometry · Droplet generation ·
Viscoelasticity · Fluid elasticity · Internal flow

1 Introduction

Particle image velocimetry techniques (PIV) have been used to study flow situation in numerous multiphase systems such as droplet dispersing, droplet evaporation, spraying, bubble flow beside, others (Raffel et al. 1998). PIV is also commonly applied to understanding complex flow behavior in different geometries under various conditions, often in combination with computational fluid dynamics.

Microfluidics utilize micrometer scaled laboratory on a chip devices to investigate the flow behavior in small fluid volumes and fluids under spatial confinement. Flow in microchannels is typically laminar and at low Reynolds numbers, since the magnitude of surface and viscous forces dominate inertial and gravity forces. Microfluidic devices are used widely for fluid dynamical investigations (Nghe et al. 2011; Schoch et al. 2008; Seemann et al. 2012; Squires and Quake 2005; Tice et al. 2003; Woerner 2012; Shui et al. 2007), cell screening and diagnostics (Auroux et al. 2002; Franke and Wixforth 2008; Haeberle and Zengerle 2007; Mark et al. 2010; Mu et al. 2013; Qi et al. 2012; Takinoue and Takeuchi 2011; Yeo et al. 2011; Gijs et al. 2010), single-molecule investigations (Dutse and Yusof 2011; Haenggi and Marchesoni 2009; Mai et al. 2012; van der Graaf et al. 2005), and templating minireactors in, e.g., biotechnology (Marques and Fernandes 2011; Song et al. 2006; Teh et al. 2008).

The simultaneous visualization of the flow behavior during the formation or deformation of droplets, either at the liquid–liquid boundaries or within in both fluid phases, has only be addressed recently, mostly due to the inherent three-dimensionality of the flow. However, the flow patterns inside a rising, falling, or static drop in a quiescent second liquid or into air was studied macroscopically by, e.g., (Horton et al. 1965; Hetsroni et al. 1970; Liu and Zheng 2006; Spells 1952; Hudson 2010). The emphasis of these works was mostly on understanding of the effect of the droplet's internal circulation on mass transfer rates

M. R. Duxenneuner · P. Fischer (✉) · E. J. Windhab
Institute of Food, Nutrition and Health, ETH Zurich,
8092 Zürich, Switzerland
e-mail: peter.fischer@hest.ethz.ch

M. R. Duxenneuner · J. J. Cooper-White (✉)
Laboratory of Tissue Engineering and Microfluidics,
Australian Institute for Bioengineering and Nanotechnology,
The University of Queensland, St Lucia, Brisbane,
QLD 4072, Australia
e-mail: j.cooperwhite@uq.edu.au

(Burkhart et al. 1976; Johnson and Hamielec 1960; Timgren et al. 2008; Dore et al. 2012; Alves et al. 2005). A number of publications deal with the internal flow pattern of liquid slugs (i.e., droplets moving along channels in contact with the channel wall) and liquid segments between neighboring slugs. For example, Thulasidas et al. (1997) observed counter-rotating vortices inside liquid segments located in between trains of bubbles utilizing high-speed video imaging and PIV. They found a correlation between the location of the vortex centers and dividing streamlines and the input liquid flow rate.

Previous work on droplet flow investigations in microchannels has been performed with droplets or bubbles moving slowly along the channel walls (Gunther et al. 2004; Kashid et al. 2005; Lindken et al. 2009; Koutsiaris et al. 1999; Schluter et al. 2008). Kinoshita et al. (2007) performed a high-speed confocal microparticle image velocimetry (μPIV) analysis to investigate the internal flow behavior of a moving droplet. They were able to measure velocity distributions of microdomain flow and obtained a three-dimensional flow structure with complex circulation patterns. The confocal μPIV technique was later extended and applied to tank-treating motion of red blood cells (Oishi et al. 2011, 2012). Dietrich et al. (2008) characterized gas–liquid flow and investigated bubble shape, size, and formation mechanism under various experimental conditions and channel geometries. Sarrazin et al. (2006) reported on numerical simulations and experimental observations of liquid–liquid flow in rectangular microchannels, focusing on interface deformation and velocity fields inside the droplets.

This paper focuses on the process of liquid–liquid dispersion, i.e., the direct injection of a disperse phase into a flowing continuous phase, a configuration that is also seen in emulsification processes, such as membrane emulsification. In particular, it investigates (1) the flow behavior inside and around a droplet during its formation when subjected to co-flow environment in microfluidic devices and (2) the influence of the viscoelasticity of the dispersed phase on the droplet detachment process. As model system, a water-in-oil emulsion composed of a food-grade aqueous biopolymer–surfactant solution as the dispersed phase (droplet) and sunflower oil as continuous (bulk) phase was used. To vary the viscoelastic properties of the droplet phase, three different concentrations of chemically modified guar gum were used (Duxenneuner et al. 2008). High molecular polymers exhibit stress relaxation properties due to the stretching and deformation of the polymer backbone under shear and elongational flow, as is present in the droplet detachment process. It is known that such relaxation phenomena substantially impact droplet formation and breakup kinetics and the final droplet size (Duxenneuner et al. 2008; Husny and Cooper-White 2006; Rodd et al.

2005a, b). The objective of the study is therefore to visualize the influence of different process and material parameters on the droplet detachment dynamics. In particular, we investigated the flow rates of both phases, the interfacial tension, and the viscoelastic properties (expressed by the polymer relaxation time) of the droplet phase. μPIV and streak imaging techniques are used to simultaneously recover the velocity profiles both within and around the dispersed phase during droplet formation and detachment, as a function of device geometry, process conditions, and material parameters.

2 Experimental setup

2.1 μPIV and streak imaging

PIV and μPIV are non-invasive optical methods for visualizing flow fields. The principle relies on the observation of tracer particles, which are either seeded into the fluid of interest or already exist within the solution. Using a double-pulsed laser, a light sheet illuminates twice a thin plane of the flowing medium. The time delay between the laser pulses depends on the mean flow velocity and the imaging magnification. The light scattered by the tracer particles is recorded on two different frames via a CCD sensor for cross-correlation. Using suitable post-processing software, the particle movement and, hence, the local vectors of particle dislocations can be determined. Since the first introduction of a μPIV system by Santiago et al. (1998), this technique has received significant attention and has been reported in numerous articles, including examples of the application of μPIV to characterize the hydrodynamic of single droplets (Tretheway and Meinhart 2002, 2004) and complex flow systems within microfluidic devices (Meinhart et al. 1999; Rodd et al. 2005a; Sarrazin et al. 2006; Williams et al. 2010). Using the streak imaging technique, the trajectories of the particles illustrate the dynamic of the fluid in the observed area and describe the flow field in and around droplets. Streak imaging summarizes the fluorescence signal of the tracer particle over longer times resulting in imaging of the streamlines of those particles.

2.2 Experimental setup

The setup for μPIV and stream imaging includes an inverse stereo microscope (Leica DM-IRB) and a workstation to control the μPIV synchronization and analysis. For streak imaging, a mercury lamp is employed as a constant illumination source for long-time exposure of the sample. The trajectories of the particles illustrate the dynamic of the system based on the Lagrangian path of the observed fluid

element. In our experiments, the 546-nm line is used to image Nile red fluorescent particles. For μPIV, two synchronized Nd:YAG lasers (double-pulsed neodymium-doped yttrium aluminum garnet crystal lasers) supplying high-intensity (400 mJ) monochrome light with a wavelength of $\lambda = 1{,}064$ nm are used. Polarization filters allow for both infrared light pulses to be doubled and vertically harmonized to a wavelength of 532 nm with pulse frequency of 30 Hz. The pulses of the light first pass through an epifluorescent prism assembly ("Y3" filter Leica). This assembly is composed of an excitation band-pass filter, which transmits λ from 500 to 560 nm, and a dichromatic mirror, which reflects $\lambda < 590$ nm and transmits $\lambda > 590$ nm. Only light with a wavelength $\lambda > 590$ nm is finally transferred to the camera detector. Depending on the experimental scale, either a microscope objective lens with magnification $20\times$ (NA0.5, long distance objective, air immersion) or $10\times$ (NA0.3, air immersion) was employed. Passing the objective, the light reaches the microscope stage where it illuminates a fluorescent particle seeded solution inside a PDMS microchannel. The fluorescent light is then reflected back to a wide spectral sensitive CCD 12-bit SensiCam QE with a 60-mm Nikkor objective (Nikon) connected to a frame grabber card. The camera has a high-speed interline data transfer cable with a dual and single readout mode. The sensor resolution is $1{,}376 \times 1{,}040$ px.

2.3 Analysis method

μPIV is a whole-flow-field technique, which provides instantaneous velocity vector measurements in a stereoscopic approach. Detailed descriptions on the μPIV algorithm and correlation techniques are given elsewhere (Meinhart et al. 2000; Olsen and Adrian 2000; Santiago et al. 1998; Sarrazin et al. 2006; Wereley et al. 2002; Williams et al. 2010). Standard μPIV relies on the velocity fields plotted in Cartesian (typically squared) space, in which all vectors are calculated using the same constant parameters (e.g., size of the interrogation area, validation setup). An individual consideration of the local geometry, changes in the local geometry, and local flow situation does not take place. The drop formation process (nucleation, growth, detachment) occurs at the capillary tip, and the multiphase flow renders the experiments inapplicable for simple averaging or cross-correlation methods. Several techniques address this shortcoming by either using a two-camera setup coupled with confocal microscopy (Kinoshita et al. 2007; Oishi et al. 2011; Park et al. 2004) or masking methods. The later technique is used by the FlexPIV algorithm (Dantec), which allows detailed analysis with multiple processing schemes of specifically defined, flexible object areas within a frame pair. To track local flow

fields in and around the droplets, the flow- and geometry-adaptive PIV processing software enables one to calculate velocity vectors in defined areas (objects) associated with an individual grid. Although it is possible to exclude certain areas from being processed by masking, the total image is still processed by the cross-correlation algorithm. Grids of different knot density can be generated and adapted specifically to the conditions of the flow field. Different processing parameters can be defined for each grid independently. As wall structures or phase boundaries cross the defined interrogation areas at oblique angles, errors in the calculated velocity vectors may occur. The possible definition of a "wall object" prohibits false calculations by disregarding the part of the interrogation area that belongs to the wall structure.

Prior to velocity field calculations, a grid needs to be defined for each object of interest. Such grid definition is provided by FlexGrid (Dantec) and offers various object geometries (rectangles, squares, ellipses, circles, and polygon curves), which can be added to the high-speed camera images. Each object can be defined as a Cartesian, polar, elliptic, or Delaunay grid. Figure 1 illustrates an example of ellipsoidal objects overlaid with a Cartesian or Delauney grid distribution. The Delauney grid system allows the fitting right to the edge of the object, unlike in the Cartesian where the grid points are distributed along horizontal and vertical lines regardless of the shape of the object.

The final processing parameters for the cross-correlation output are designated to each grid individually. The Flex-PIV and Flexgrid software links the defined object with additional properties such as "grid" (main object to cross-correlate using a specific local grid and analysis function, calculation results in vector fields), "hole" (usually combined with the grid object to mark a grid-less area with no correlation), "false hole" (local grid parameters can be set and will be considered for the cross-correlation, no vector indication), or "wall" (solid area with no flow at all and therefore with no grid subdivision; the part of the interrogation area that is inside the wall will be masked out by the correlation function). An example is given in Fig. 2.

We performed FlexPIV analysis utilizing an adaptive correlation algorithm with interrogation area overlap of at least 25–50 %. To avoid strong velocity gradients, the software allows the change in interrogation area size and shape, employing different coordinate arrangements (Cartesian or Delauney) with radial or triangular connectivity. In our case, the interrogation area is sized at either 16×16 px or 32×32 px, depending on the velocity flow fields, leading to velocity variations of 5–10 % within the interrogation area. Further post-processing procedures were kept to a minimum for all μPIV experiments. The area outside the actual microchannel was masked out prior to

Fig. 1 Cartesian (*top*) and Delauney (*bottom*) grid distribution (*left*) and the specific FlexPIV triangular vector connectivity (*right*). The triangular connectivity allows each vector point 6 neighbors for peak validation. The origin (0/0) of both grids is chosen to be in the *left*, *bottom corner*
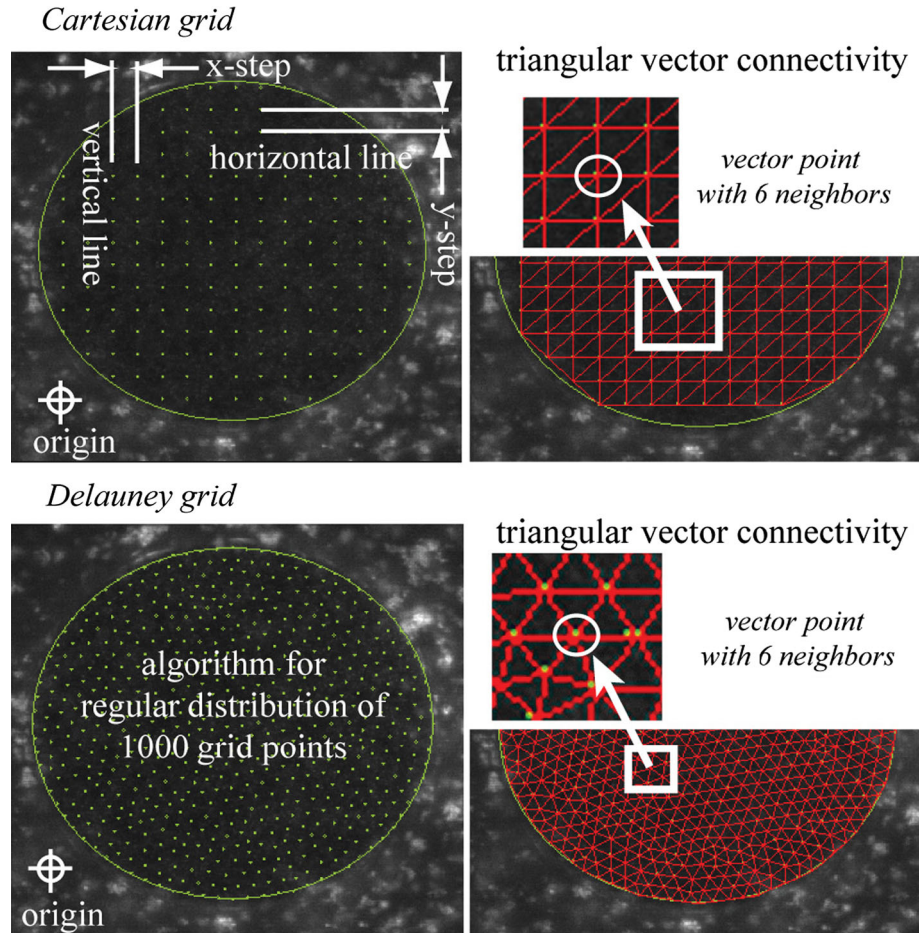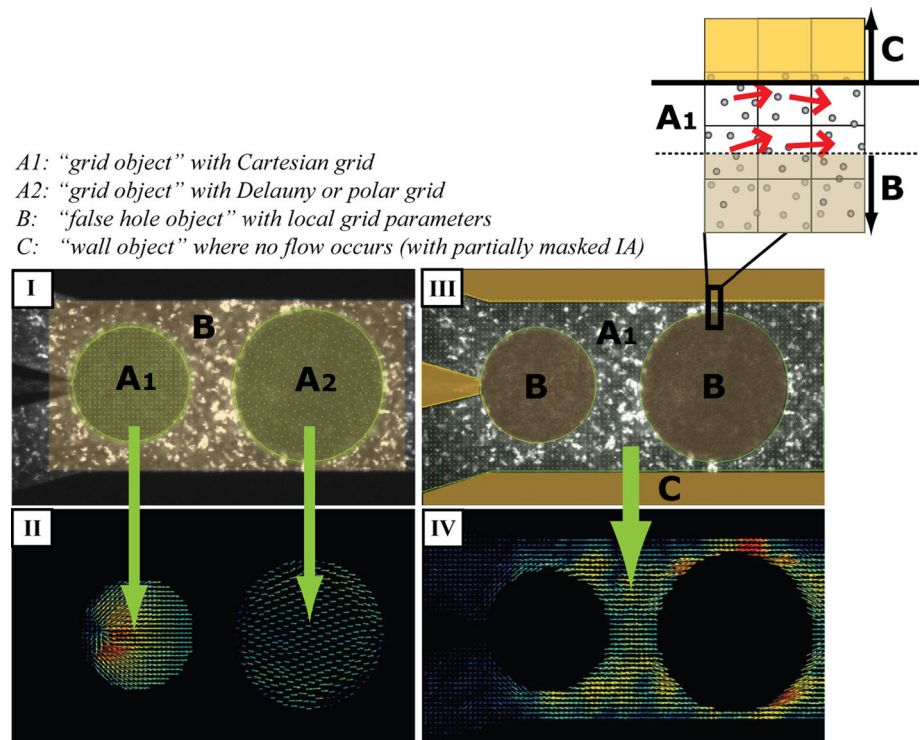
Fig. 2 Specification of object areas for simultaneous FlexPIV analysis: *Image I* shows the fluorescence picture of the droplet phase, while *Image II* depicts the flow-field calculation inside the droplet neglecting the flow of the surrounding continuous phase. *Images III* and *IV* show the same procedure for the bulk fluid phase neglecting the droplet phase. Analysis is performed using FlexPIV using the "hole" and "false hole" masking

A1: "grid object" with Cartesian grid
A2: "grid object" with Delauny or polar grid
B: "false hole object" with local grid parameters
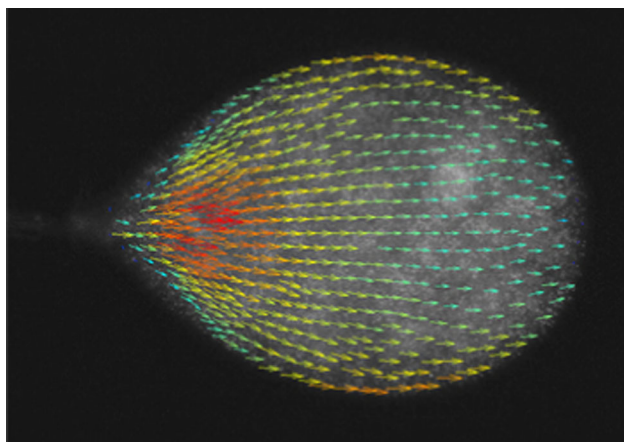C: "wall object" where no flow occurs (with partially masked IA)

Fig. 3 Fluorescent micrograph matched with the corresponding vector field to verify the resultant cross-correlation analysis

FlexPIV analysis to minimize the number of false velocity vectors. In order to verify the result of the cross-correlation, the original fluorescent micrograph and the corresponding velocity vector field were matched, as shown in Fig. 3.

3 Material

3.1 PDMS microchannel and geometries

PDMS-based co-flow devices with different capillary geometries and sizes were manufactured using standard soft lithography techniques. With this fabrication method, we were able to produce geometrically similar channels with a capillary outlet diameter (which was varied between 0.01 and 0.02 mm) and channel height of $h_{cl} \approx 0.2 \pm 0.01$ mm. In order to calculate the hydrodynamic diameters of both the channels, Dh_{cl}, and the capillaries, Dh_{cp}, and thus, the actual velocity of the both phases, the actual h_{cl} was verified prior experimental performance. Figure 4 shows the utilized microfluidic channel with pointed capillary tip with
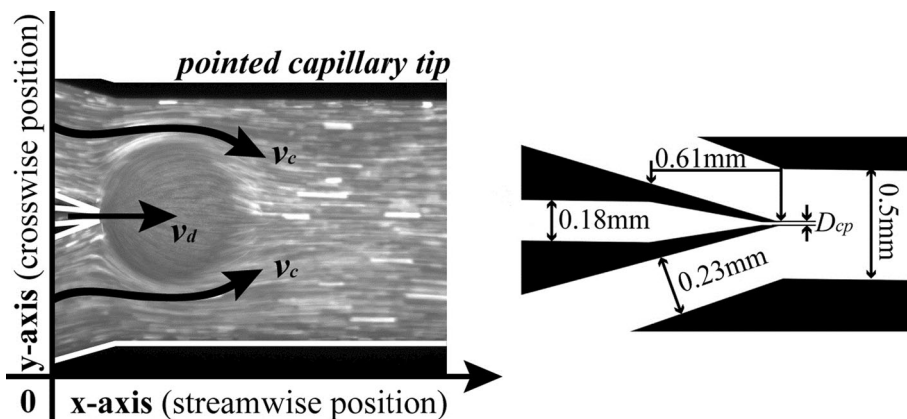
$D_{cp,in} = D_{cp,out} = 0.033$ mm. The effective hydraulic channel diameter, $Dh_{cl,eff} = Dh_{cl} - Dh_{cp,out}$, is 0.13 mm.

The flow direction of both phases is parallel to the nominated direction of the x axis. The width of the microchannel is given by the y axis and the height of the channel by the z axis. The position of the droplet is described by the flow position (x axis) and crosswise position (y axis). The flow rate of the disperse phase, Q_{disp}, was set at values between 0.01 and 1.0 ml/h, whereas the flow rate of the continuous oil phase was varied between $0.1 \leq Q_{cont} \leq 5.0$ ml/h. Both fluids were delivered to the microdevice via microbore tubing (PE50 Intramedic, outer diameter = 1.5 mm, inner diameter = 0.5 mm) and stainless steel connectors (22 gauge, outer diameter ≈ 0.71 mm) using constant displacement rate syringe pumps (Harvard PhD 2000). Inlet and outlet ports were located ~ 30 mm up stream and downstream of the droplet generation zone.

3.2 Fluids

As continuous phase, cold-pressed sunflower oil (Florin AG, Switzerland) is used in all experiments. Sunflower oil exhibits Newtonian flow behavior with viscosity of 56 mPas ($T = 20$ °C), density of ≈ 0.916 g/cm^3, and interfacial tension (water in sunflower oil) of about 23 mN/m. As the dispersed phase, two aqueous solutions were used throughout this study: A Newtonian solution composed of distilled water with non-ionic Tween 20 surfactants (polyoxyethylene sorbate) at concentrations from 0 (pure water) to 0.893 wt%. The interfacial tension of the different solutions is summarized in Table 1. The density and the viscosity of the aqueous Tween 20 solutions are considered to be those of water (~ 1.000 g/cm^3, ~ 1 mPas). To study the droplet formation for elastic fluids, non-Newtonian solutions hydrophobically modified guar gum (hydroxypropyl-ether guar gum (HPGG), Rhodia) were added to the water–surfactant phase in the concentration regime of 0.01–0.2 wt% (see Table 1). The

Fig. 4 Illustration of the PDMS-based microfluidic channel geometries with pointed orifice and thin outlet wall

viscoelastic behavior of HPGG solutions has been described by Duxenneuner et al. (2008), and a brief summary of the material properties is given in the following. Guar gum is a high molecular weight polysaccharide extracted from Cyamopsis tetragonolobus seeds and widely used as a stabilizing and thickening agent in food, pharmaceutical, and personal care products, as well as dying liquor and in enhanced oil recovery. Guar gum is non-ionic and composed from a D-mannose backbone decorated with branches of D-galactose units in a statistical fashion. Chemical modification leads to better solubility, resistance to shear degradation, salt tolerance, faster hydration rate, and better temperature stability. The used HPGG exhibits Newtonian flow properties under shear flow at concentrations up to 0.1 wt% and shear thinning behavior at higher concentrations. Solutions used in this investigations are in the transition regime between diluted and semi-dilute regimes, i.e., in the regime of the overlap concentration and therefore responsive to stress relaxation mechanisms of the deformed polymer chain. In this concentration regime, shear and elongational viscosity as well as the polymer relaxation time exhibit different scaling behaviors. The transitional concentration regime was chosen because the presence of high molecular polymer is known to substantially impact droplet formation and breakup kinetics and final droplet size within microfluidic devices (Duxenneuner et al. 2008; Husny and Cooper-White 2006; Rodd et al. 2005a, b).

For all experiments, either one or both phases were seeded with fluorescent particles of various sizes. We used carboxylated polystyrene microspheres from Duke Scientific (R100, R300, R500, R700, Nile red, suspended in H_2O) as fluorescent tracer particles with an excitation $\lambda_{ex,max} = 542$ nm and emission maximum wavelength $\lambda_{em,max} = 612$ nm, respectively. The particle diameter varied from $D_{R100} = 0.10$ μm, $D_{R300} = 0.30$ μm, $D_{R500} = 0.49$ μm, and $D_{R700} = 0.71$ μm depending on the geometrical constraints of the microfluidic device. The

seeding particle concentrations were optimized to allow for the capture of in-focus particles over the background "glow" (0.05 vol % for tracer particle smaller than 0.7 mm diameter and 0.03 vol % for particles with diameter ≥0.7 mm). This was particularly relevant when using deep microchannels, where the background illumination increases rapidly with increasing number of out-of-focus particles.

4 Results and discussion

The droplet formation in the dripping regime can be divided in three different stages: (1) filling: the droplet is attached to the capillary outlet and expands in all directions until the equilibrium of the net forces is lost (interfacial tension vs. detaching forces), (2) necking: droplet separation, which starts by forming a neck, and (3) pinch-off: the neck thins rapidly until the droplet finally pinches off (drag and inertial forces overcome the interfacial tension force, (Cramer et al. 2004)). The influence of the added biopolymer, i.e., the influence of the viscoelasticity expressed by the polymer relaxation time, is depicted in Fig. 5 where the droplet detachment of the pure aqueous phase (0.161 wt% Tween 20) and the viscoelastic biopolymer phase (0.161 wt% Tween 20, 0.2 wt% HPGG) are compared. While the Newtonian droplets detached in a purely dripping mode, viscoelastic droplets form an elongated neck or filament prior to detachment.

Figure 6a visualizes the evolution of a purely aqueous droplet (0.161 wt% Tween 20) at the capillary tip. Streak imaging is used to investigate qualitatively the flow of the ambient phase around the capillary tip and in the droplet. Even though the disperse phase is also seeded with tracer particles (Fig. 6a), no distinct particle motion inside the droplet is observed. On the other hand, we observed the onset of symmetrical vortices on each side of the capillary

Table 1 Interfacial tension of aqueous Tween 20 and aqueous Tween 20–HPGG solutions at 23 °C

Solution	cTween (wt%)	cHPGG (wt%)	γ (mN/m)	Θ^* (ms)	η_{ext}^* (Pas)
Water	–	–	23.6	–	–
Tween 20	0.161	–	15.3	–	–
Tween 20	0.228	–	9	–	–
Tween 20	0.893	–	7	–	–
HPGG	–	0.01	8.4	0.937	0.53
HPGG	–	0.1	2.8	2.047	1.43
HPGG	–	0.2	1.9	4.754	1.49
Tween 20–HPGG	0.161	0.01	6.2	–	–
Tween 20–HPGG	0.161	0.1	4.3	–	–
Tween 20–HPGG	0.161	0.2	2.7	–	–
Tween 20–HPGG	0.228	0.1	1.9	–	–
Tween 20–HPGG	0.893	0.1	1.7	–	–

* Polymer relaxation time Θ and extensional viscosity η_{ext} are taken from Duxenneuner et al. (2008)

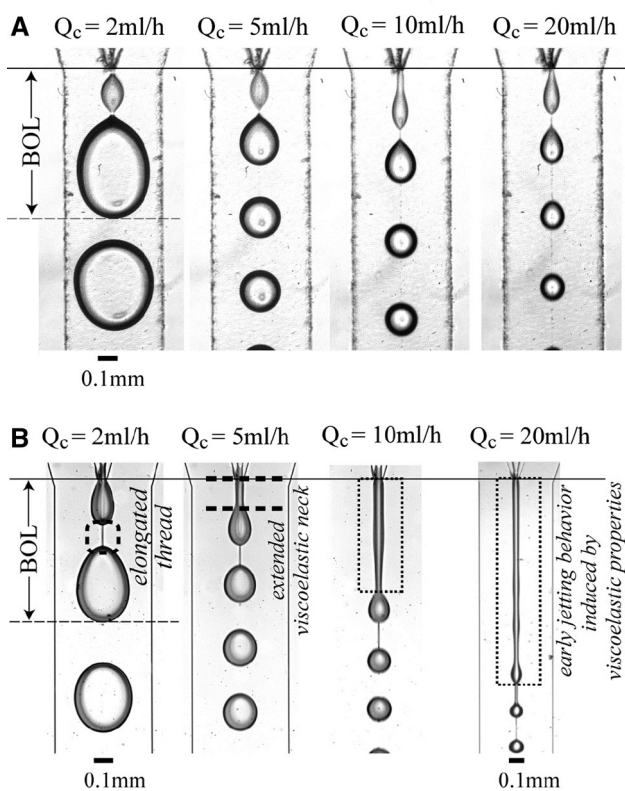**Fig. 5 a** Droplet detachment of a Newtonian water droplet (0.161 wt% Tween 20) and **b** a viscoelastic droplet (0.161 wt% Tween 20, 0.2 wt% HPGG) into sunflower oil (Q_{disp} = 0.1 ml/h, Q_{cont} = 2.0–20.0 ml/h, *BOL* break-off length)

outlet at the beginning of droplet formation process. Images in Fig. 6a show that the disperse phase leaving the orifice and the formation of the droplet disturbs the flow of the continuous phase. This leads to vortices (Fig. 6a-ii), which disappear with progressive droplet filling, necking, and final pinch-off. The drag force imposed by the bulk phase encourages the detachment of the droplet from the orifice. With increasing velocity of the continuous phase, v_{cont}, (at constant velocity of the disperse phase v_{disp}), the initial vortex area grows larger. An increase of v_{disp} (at constant velocity of the continuous phase v_{cont}) results in slower droplet formation and an increase in the final droplet size (Cramer et al. 2004). The impact of the drag force decreases and has less influence on the deformation of the droplet shape.

In Fig. 6b, experiments inside the same microfluidic channel at similar flow rates as Fig. 6a (Q_{disp} = 0.01 ml/h (v_{disp} = 0.08 m/s) and Q_{cont} = 0.1 ml/h (v_{cont} = 0.03 m/s)) are depicted for the viscoelastic aqueous dispersed phase (0.161 wt% Tween 20 and 0.2 wt% HPGG). The increased viscoelasticity, i.e., the increased concentration of HPGG (see Table 1 for polymer relaxation time and extensional viscosity) of the disperse phase, results in a longer neck (see Fig. 6b-v) being formed between the

nozzle outlet and the leading edge of the dispersed phase during the evolution of the droplet. This behavior is as expected for a viscoelastic droplet of low interfacial tension in a Newtonian bulk phase. This neck leads to droplet pinch-off occurring further downstream from the capillary outlet (compared to the non-viscoelastic solution), which provides for a smoother geometrical form of the droplet when attached to the capillary. Hence, the bulk phase flow path is less perturbed by the presence of the neck and does not form large vortices.

Employing µPIV we were able to visualize the inner and outer velocity profiles of the droplet forming in co-flowing sunflower oil. Figure 7 presents a water droplet within the microfluidic channel at the stage of filling (Row A), prior to necking (Row B), and just before pinching-off (Row C). The experiment was run at flow rates of Q_{disp} = 0.1 ml/h (v_{disp} = 0.83 m/s) and Q_{cont} = 0.5 ml/h (v_{cont} = 0.17 m/s). The time between the laser pulses was set to dt = 0.1 ms. The fluorescent micrographs (Fig. 7, left column) and the high-speed analysis (inserts,) show the captured frames of the fluorescent droplet and its actual position inside the microfluidic channel. As shown by the different colors of the velocity vectors, one can clearly observe that the speed of the disperse phase is fastest near the capillary outlet and much faster than the velocity of the ambient fluid (Fig. 7, middle column). With increasing distance from the orifice, the droplet velocity decreases, adjusting to the flow of the ambient fluid. Figure 7 (right column) shows the velocity inside the droplet as a function of the downstream position (y axis). To analyze the flow profile quantitatively, the velocity values of the droplet were taken at four different positions along the x axis (downstream positions). The symmetrical velocity distribution at various locations shows a decrease with increasing droplet size and with increasing distance from the capillary tip.

In Fig. 8, two pure water droplets are compared in the same channel geometry at a similar evolution stage but different velocity v_{cont} (doubling from v_{cont} = 0.08 m/s (Fig. 8a) to v_{cont} = 0.17 m/s (Fig. 8b)). The size of the droplet in Fig. 8b is slightly smaller due to the higher velocity, and thus, the droplet formation time is shorter. The graphics on the right column in Fig. 8 illustrate clearly the increase in the velocity values for both settings. Comparing the velocity field of each droplet at the same marked positions inside the droplet, we recognize that the values for v_{cont} = 0.17 m/s are almost twice the corresponding value for v_{cont} = 0.08 m/s.

Figure 9 illustrates the streak image (top), vector profile (middle), and the contour plot (bottom) of the velocity field of the ambient bulk fluid flowing around a droplet forming at the pointed capillary tip (left column) and around a droplet flowing along the channel (right column).

Fig. 6 **a** Streak images of a Newtonian water droplet (0.161 wt% Tween 20) into sunflower oil at various stages during formation ($Q_{disp} = 0.01$ ml/h, $Q_{cont} = 0.1$ ml/h). **b** Streak images of a viscoelastic droplet (0.161 wt% Tween 20, 0.2 wt% HPGG) into sunflower oil at various formation stages ($Q_{disp} = 0.01$ ml/h, $Q_{cont} = 0.1$ ml/h)
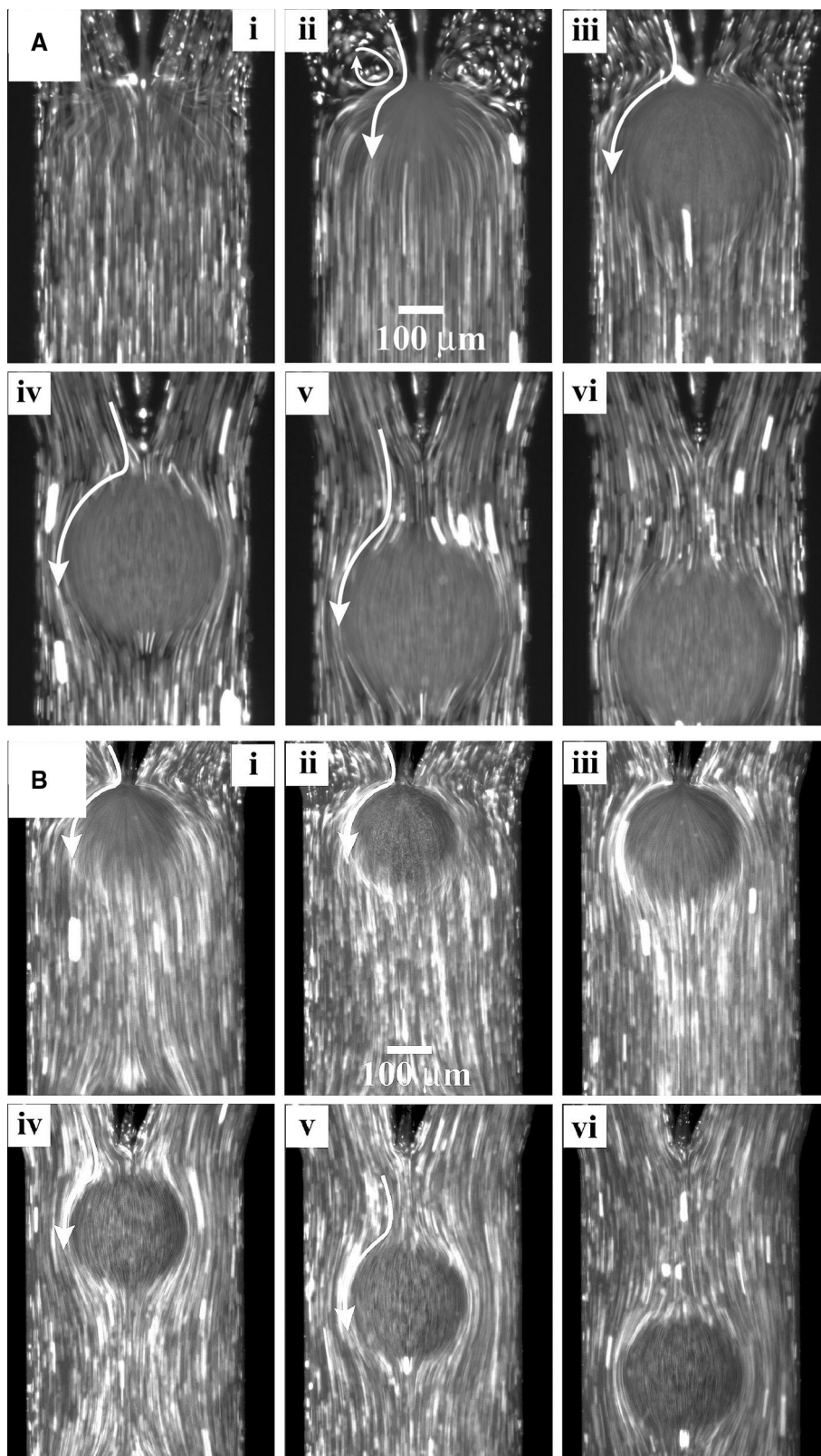
The flow velocity ratio for this experiment was set to $v_{disp} = 0.08$ m/s and $v_{cont} = 0.03$ m/s ($Q_{disp} = 0.01$ ml/h, $Q_{cont} = 0.1$ ml/h). With FlexPIV, we were able to extract the velocity information from the bulk phase by marking out the drop as a "false hole" object. As the droplet is still attached to the orifice, it fills the channel volume and
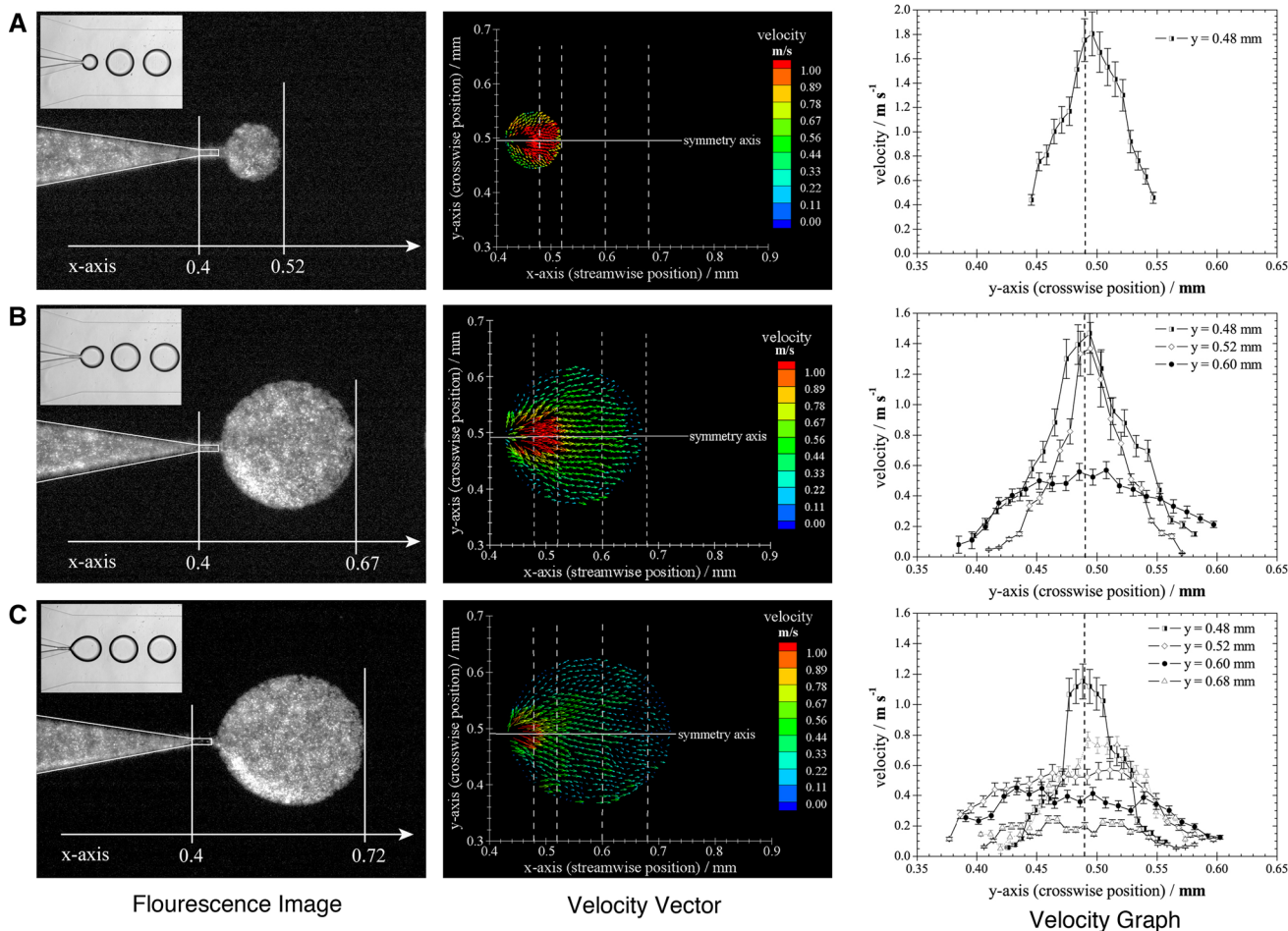
Fig. 7 Fluorescent micrographs (*left column*), velocity vector fields (*middle column*), and corresponding velocity graphs (*right column*) of the flow behavior of a forming water droplet ($Q_{disp} = 0.1$ ml/h) in sunflower oil ($Q_{cont} = 0.5$ ml/h) generated at the pointed capillary tip (*images* in row A, B, and C shown the droplet formation at different times, µPIV settings: scaling factor SF = 0.138; $dt = 0.1$ ms; R700 tracer particles in the aqueous dispersed phase, flow direction from *left* to *right*)

blocks the continuous phase flow. After the droplet pinch-off, the final volume of the droplet fills the channel and narrows the remaining space for the continuous phase fluid. Following the equation of continuity, the velocity of the continuous phase fluid has to increase drastically to maintain the volumetric flow rate with decreasing available space. As shown in both cases (left and right column), the continuous phase passes the narrow gap between the droplet and the channel wall with increased velocity. The rising bulk velocity causes an increase in the viscous drag force, which supports the detachment of the droplet from the capillary.

Figure 10 shows a viscoelastic droplet (Tween 20–HPGG solutions) just prior pinch-off. The viscoelasticity of the dispersed phase results in the formation of an elongated neck or filament. The velocity ratio is $v_{disp}/v_{cont} = 4.8$ with $Q_{disp} = 1$ ml/h ($v_{disp} = 8.3$ m/s) and $Q_{cont} = 5$ ml/h ($v_{disp} = 1.7$ m/s). Figure 10 shows the difference in the velocity profile of the same droplet but at various levels of

object planes (close to the top, in the middle, and near the bottom of the droplet). The actual velocity at similar downstream positions differs from height level to height level. In early stages of the droplet generation, i.e., as long as the droplet is fully attached to the capillary, the flow of the disperse fluid is filling the droplet constantly and the emerging inertial force leads to a volume extension of the droplet mainly in direction of the flow stream, a similar behavior as seen for Newtonian droplets in Fig. 7. However, in the later stage of droplet formation and unlike the Newtonian droplet pinching-off, the viscoelastic droplet is still attached to the capillary tip via the filament. At this stage of the droplet formation almost no fluid is transported through the filament to the droplet, a phenomenon also found in extensional experiments on liquid bridges (e.g., CaBER experiments) (Gier and Wagner 2012). The fluorescent particles only indicate a movement away from the filament to the downstream end of the droplet where they remain until the droplet breaks off.

Fig. 8 Velocity vector field
(*left column*) and velocity graph
(*right column*) of pure water
droplet formation into sunflower
oil at a pointed capillary tip at
a $Q_{disp} = 0.01$ ml/h and
$Q_{cont} = 0.1$ ml/h ($v_c = 0.08$ m/
s) and at **b** $Q_{disp} = 0.1$ ml/h and
$Q_{ccont} = 0.5$ ml/h
($v_{cont} = 0.17$ m/s)

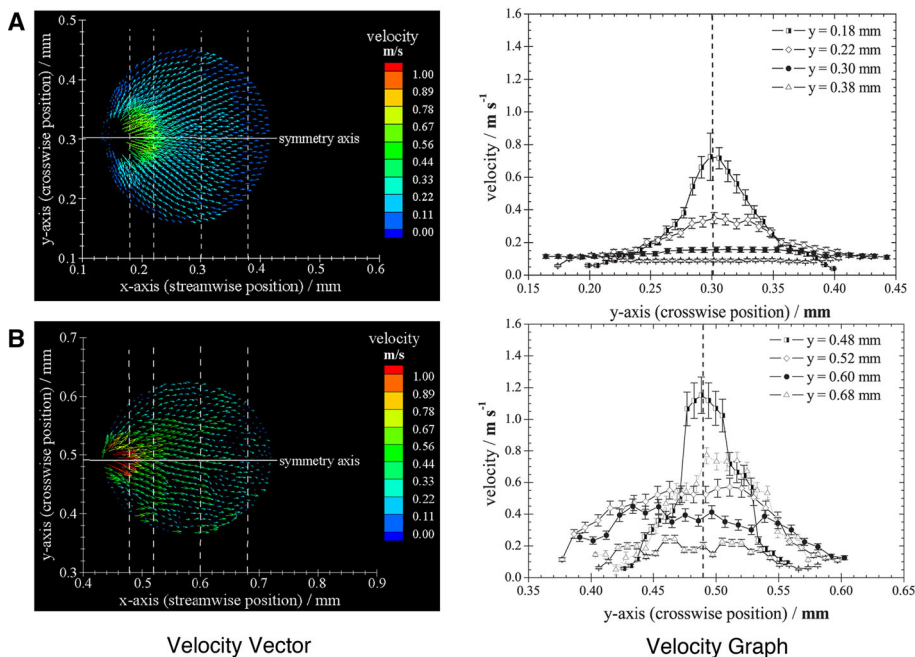**Velocity Vector**   **Velocity Graph**

Fig. 9 FlexPIV analysis
(**a** fluorescence image,
b velocity vector, **c** velocity
contour plot) of the outer
velocity field of a pure water
droplet growing at the capillary
(*left column*) and flowing along
the channel (*right column*). Both
phases are seeded with particles
(R700 in H2O and R100 in
sunflower oil). The velocity
ratio is $v_{disp} = 0.08$ m/s and
$v_{cont} = 0.03$ m/s with
$Q_{disp} = 0.01$ ml/h and
$Q_{cont} = 0.1$ ml/h (μPIV
settings: scaling factor
SF = 0.093, d$t = 1.0$ ms)

At Capillary   **In Channel**
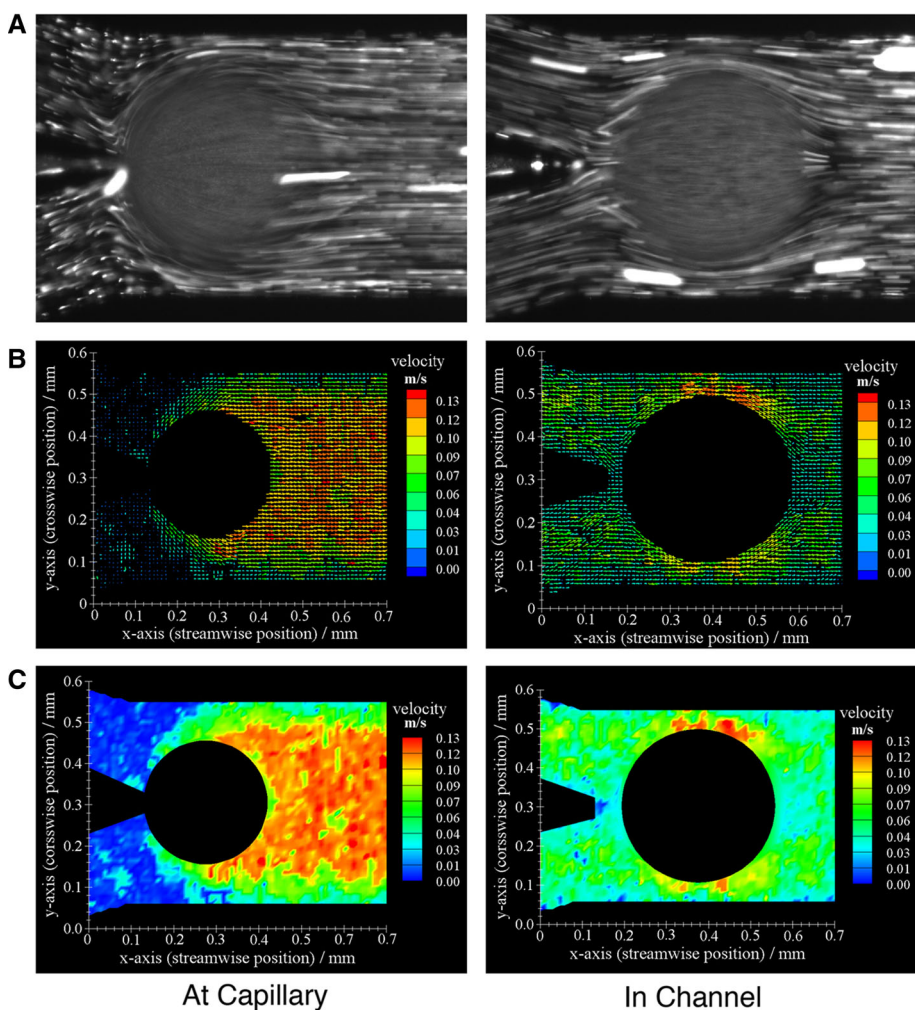
Fig. 10 Velocity vector fields (*left column*) and corresponding velocity contour plots of different focus levels of a forming viscoelastic droplet (0.161 wt% Tween 20, 0.2 wt% HPGG, Q_{disp} = 1.0 ml/h) into sunflower oil (Q_{cont} = 5.0 ml/h). The object focus was set at different droplet height (**a** upper droplet, **b** drop equator, **c** lower droplet). The droplet was captured just prior pinching-off (µPIV settings: scaling factor SF = 0.138, dt = 0.5 ms, h_{cl} = 0.22 mm, d_p = 0.71 mm)

Velocity Vector   Velocity Field
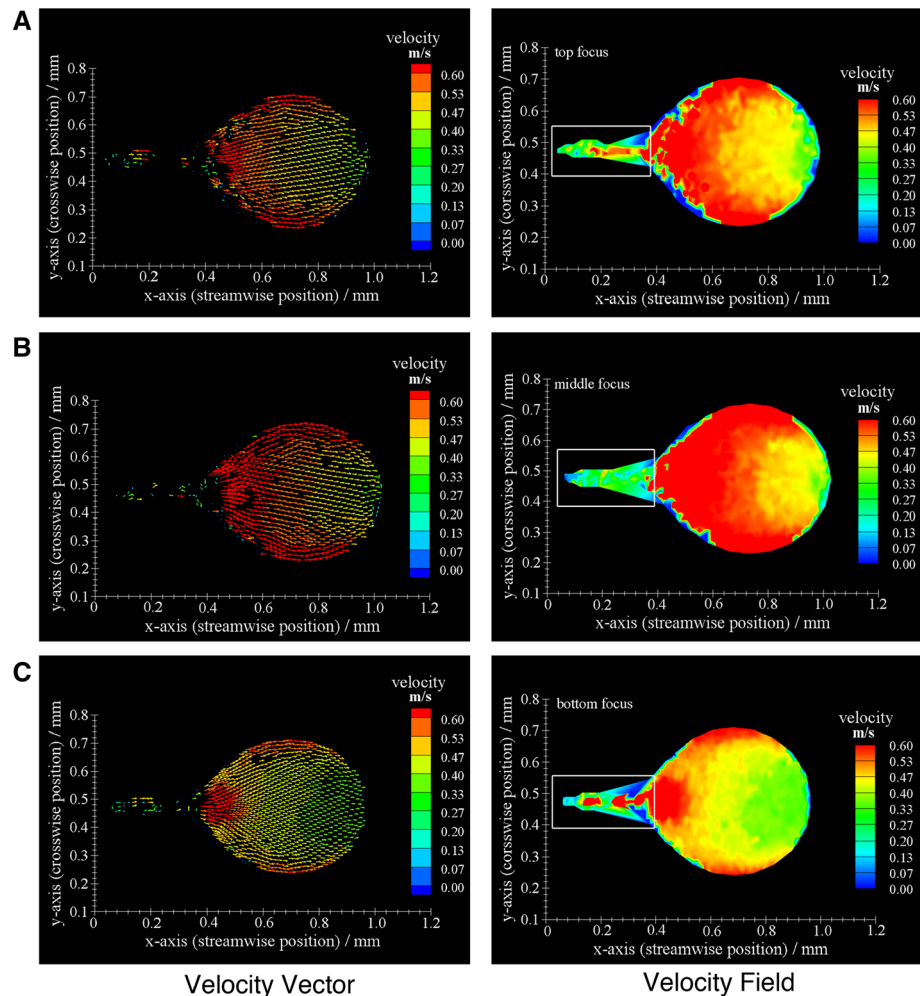
5 Conclusion

Droplet generation of Newtonian and non-Newtonian (elastic) fluids into oil in co-flowing microfluidic channels was investigated with µPIV, focusing on the simultaneous observation of the flow inside and around the forming droplet. Both the dispersed phase solutions (mixtures of Tween and hydroxypropylether guar gum) and the continuous phase (sunflower oil) were successfully seeded with the same fluorescent particles. Through the application of flexible grids (FlexPIV and Flex-Grid), the images were used to analyze both the inner and outer fluid flows, i.e., to map the entire flow situation produced as a result of the device geometry, process conditions, and fluid parameters. The flow pattern of the surrounding sunflower oil is dominated by the downstream flow, but shows, depending on the formation stage of the droplet, steady through to unsteady (vortex) flows. Velocity profiles and the corresponding fluorescent micrographs of the inner flow behavior of the forming droplets show a rapidly expanding flow when close to the capillary tip through to a quiescent flow situation at the leading edge of the droplet. With increasing droplet age, i.e., at the stage if droplet detachment, the difference of the

internal field strengths levels out. The influence of viscoelastic fluid properties on the droplet detachment process confirmed that the polymer stress relaxation properties of the high molecular weight HPGG lead to filament formation prior to droplet detachment, resulting in substantial changes to the flow behavior within the neck and within the attached droplet. Internal fluid recirculation in the droplet was not observed in any stage of droplet formation (initiation, growth, and detachment), indicating a flow situation that seeks a low stress situation with the surrounding continuous phase.

References

Alves SS, Orvalho SP, Vasconcelos JMT (2005) Effect of bubble contamination on rise velocity and mass transfer. Chem Eng Sci 60(1):1–9. doi:10.1016/j.ces.2004.07.053

Auroux PA, Iossifidis D, Reyes DR, Manz A (2002) Micro total analysis systems. 2. Analytical standard operations and applications. Anal Chem 74(12):2637–2652. doi:10.1021/ac020239t

Burkhart L, Weathers PW, Sharer PC (1976) Mass-transfer and internal circulation in forming drops. AIChE J 22(6):1090–1096. doi:10.1002/aic.690220620

Cramer C, Fischer P, Windhab EJ (2004) Drop formation in a co-flowing ambient fluid. Chem Eng Sci 59:3045–3058

Dietrich N, Poncin S, Midoux N, Li HZ (2008) Bubble formation dynamics in various flow-focusing microdevices. Langmuir 24(24):13904–13911. doi:10.1021/la802008k

Dore V, Tsaoulidis D, Angeli P (2012) Mixing patterns in water plugs during water/ionic liquid segmented flow in microchannels. Chem Eng Sci 80:334–341. doi:10.1016/j.ces.2012.06.030

Dutse SW, Yusof NA (2011) Microfluidics-based lab-on-chip systems in DNA-based biosensing: an overview. Sensors 11(6):5754–5768. doi:10.3390/s110605754

Duxenneuner MR, Fischer P, Windhab EJ, Cooper-White JJ (2008) Extensional properties of hydroxypropyl ether guar gum solutions. Biomacromolecules 9:2989–2996

Franke TA, Wixforth A (2008) Microfluidics for miniaturized laboratories on a chip. ChemPhysChem 9(15):2140–2156. doi:10.1002/cphc.200800349

Gier S, Wagner C (2012) Visualization of the flow profile inside a thinning filament during capillary breakup of a polymer solution via particle image velocimetry and particle tracking velocimetry. Phys Fluids 24(5):053102

Gijs MAM, Lacharme F, Lehmann U (2010) Microfluidic applications of magnetic particles for biological analysis and catalysis. Chem Rev 110(3):1518–1563. doi:10.1021/cr9001929

Gunther A, Khan SA, Thalmann M, Trachsel F, Jensen KF (2004) Transport and reaction in microscale segmented gas-liquid flow. Lab Chip 4(4):278–286. doi:10.1039/b403982c

Haeberle S, Zengerle R (2007) Microfluidic platforms for lab-on-a-chip applications. Lab Chip 7(9):1094–1110. doi:10.1039/b706364b

Haenggi P, Marchesoni F (2009) Artificial Brownian motors: controlling transport on the nanoscale. Rev Mod Phys 81(1):387–442. doi:10.1103/RevModPhys.81.387

Hetsroni G, Haber S, Wacholde E (1970) Flow fields in and around a droplet moving axially within a tube. J Fluid Mech 41:689. doi:10.1017/s0022112070000848

Horton TJ, Fritsch TR, Kintner RC (1965) Experimental determination of circulation velocities inside drops. Can J Chem Eng 43(3):143–146

Hudson SD (2010) Poiseuille flow and drop circulation in microchannels. Rheol Acta 49(3):237–243. doi:10.1007/s00397-009-0394-4

Husny J, Cooper-White JJ (2006) The effect of elasticity on drop creation in T-shaped microchannels. J Nonnewton Fluid Mech 137(1–3):121–136

Johnson AI, Hamielec AE (1960) Mass transfer inside drops. AIChE J 6(1):145–149. doi:10.1002/aic.690060128

Kashid MN, Gerlach I, Goetz S, Franzke J, Acker JF, Platte F, Agar DW, Turek S (2005) Internal circulation within the liquid slugs of a liquid–liquid slug-flow capillary microreactor. Ind Eng Chem Res 44(14):5003–5010. doi:10.1021/ie0490536

Kinoshita H, Kaneda S, Fujii T, Oshima M (2007) Three-dimensional measurement and visualization of internal flow of a moving droplet using confocal micro-PIV. Lab Chip 7(3):338–346. doi:10.1039/b617391h

Koutsiaris AG, Mathioulakis DS, Tsangaris S (1999) Microscope PIV for velocity-field measurement of particle suspensions flowing inside glass capillaries. Meas Sci Technol 10(11):1037–1046. doi:10.1088/0957-0233/10/11/311

Lindken R, Rossi M, Grosse S, Westerweel J (2009) Micro-particle image velocimetry (mu PIV): recent developments, applications, and guidelines. Lab Chip 9(17):2551–2567. doi:10.1039/b906558j

Liu ZL, Zheng Y (2006) PIV study of bubble rising behavior. Powder Technol 168(1):10–20

Mai DJ, Brockman C, Schroeder CM (2012) Microfluidic systems for single DNA dynamics. Soft Matter 8(41):10560–10572. doi:10.1039/c2sm26036k

Mark D, Haeberle S, Roth G, von Stetten F, Zengerle R (2010) Microfluidic lab-on-a-chip platforms: requirements, characteristics and applications. Chem Soc Rev 39(3):1153–1182. doi:10.1039/b820557b

Marques MPC, Fernandes P (2011) Microfluidic devices: useful tools for bioprocess intensification. Molecules 16(10):8368–8401. doi:10.3390/molecules16108368

Meinhart CD, Wereley ST, Santiago JG (1999) PIV measurements of a microchannel flow. Exp Fluids 27(5):414–419

Meinhart CD, Wereley ST, Santiago JG (2000) A PIV algorithm for estimating time-averaged velocity fields. J Fluids Eng Trans Asme 122(2):285–289

Mu X, Zheng W, Sun J, Zhang W, Jiang X (2013) Microfluidics for manipulating cells. Small 9(1):9–21. doi:10.1002/smll.201200996

Nghe P, Terriac E, Schneider M, Li ZZ, Cloitre M, Abecassis B, Tabeling P (2011) Microfluidics and complex fluids. Lab Chip 11(5):788–794. doi:10.1039/c0lc00192a

Oishi M, Kinoshita H, Fujii T, Oshima M (2011) Simultaneous measurement of internal and surrounding flows of a moving droplet using multicolour confocal micro-particle image velocimetry (micro-PIV). Meas Sci Technol 22(10). doi:10.1088/0957-0233/22/10/105401

Oishi M, Utsubo K, Kinoshita H, Fujii T, Oshima M (2012) Continuous and simultaneous measurement of the tank-treading motion of red blood cells and the surrounding flow using translational confocal micro-particle image velocimetry (micro-PIV) with sub-micron resolution. Meas Sci Technol 23(3):35301

Olsen MG, Adrian RJ (2000) Brownian motion and correlation in particle image velocimetry. Opt Laser Technol 32(7–8):621–627

Park JS, Choi CK, Kihm KD (2004) Optically sliced micro-PIV using confocal laser scanning microscopy (CLSM). Exp Fluids 37(1):105–119. doi:10.1007/s00348-004-0790-6

Qi D, Hoelzle DJ, Rowat AC (2012) Probing single cells using flow in microfluidic devices. Eur Phys J Special Top 204(1):85–101. doi:10.1140/epjst/e2012-01554-x

Raffel M, Willert CE, Kompenhans J (1998) Particle image velocimetry—a practical guide. Experimental fluid mechanics, 3rd edn. Springer, Berlin

Rodd LE, Scott TP, Boger DV, Cooper-White JJ, McKinley GH (2005a) The inertio-elastic planar entry flow of low-viscosity elastic fluids in micro-fabricated geometries. J Nonnewton Fluid Mech 129(1):1–22

Rodd LE, Scott TP, Cooper-White JJ, McKinley GH (2005b) Capillary break-up rheometry of low-viscosity elastic fluids. Appl Rheol 15(1):12–27

Santiago JG, Wereley ST, Meinhart CD, Beebe DJ, Adrian RJ (1998) A particle image velocimetry system for microfluidics. Exp Fluids 25(4):316–319

Sarrazin F, Loubiere K, Prat L, Gourdon C, Bonometti T, Magnaudet J (2006) Experimental and numerical study of droplets hydro-dynamics in microchannels. AIChE J 52(12):4061–4070

Schluter M, Hoffmann M, Rabiger N (2008) Characterization of microfluidic devices by measurements with mu-PIV and CLSM. Part Image Velocim New Dev Recent Appl 112:19–33

Schoch RB, Han J, Renaud P (2008) Transport phenomena in nanofluidics. Rev Mod Phys 80(3):839–883. doi:10.1103/RevModPhys.80.839

Seemann R, Brinkmann M, Pfohl T, Herminghaus S (2012) Droplet based microfluidics. Rep Prog Phys 75(1). doi:10.1088/0034-4885/75/1/016601

Shui L, Eijkel JCT, van den Berg A (2007) Multiphase flow in microfluidic systems—control and applications of droplets and interfaces. Adv Colloid Interface Sci 133(1):35–49. doi:10.1016/j.cis.2007.03.001

Song H, Chen DL, Ismagilov RF (2006) Reactions in droplets in microfluidic channels. Angewandte Chemie Int Edition 45(44):7336–7356. doi:10.1002/anie.200601554

Spells KE (1952) A study of circulation patterns within liquid drops moving through a liquid. Proc Phys Soc Lond Sect B 65(391):541. doi:10.1088/0370-1301/65/7/310

Squires TM, Quake SR (2005) Microfluidics: fluid physics at the nanoliter scale. Rev Mod Phys 77(3):977–1026. doi:10.1103/RevModPhys.77.977

Takinoue M, Takeuchi S (2011) Droplet microfluidics for the study of artificial cells. Anal Bioanal Chem 400(6):1705–1716. doi:10.1007/s00216-011-4984-5

Teh SY, Lin R, Hung LH, Lee AP (2008) Droplet microfluidics. Lab Chip 8(2):198–220. doi:10.1039/b715524g

Thulasidas TC, Abraham MA, Cerro RL (1997) Flow patterns in liquid slugs during bubble-train flow inside capillaries. Chem Eng Sci 52(17):2947–2962. doi:10.1016/s0009-2509(97)00114-0

Tice JD, Song H, Lyon AD, Ismagilov RF (2003) Formation of droplets and mixing in multiphase microfluidics at low values of the Reynolds and the capillary numbers. Langmuir 19(22):9127–9133. doi:10.1021/la030090w

Timgren A, Tragardh G, Tragardh C (2008) Application of the PIV technique to measurements around and inside a forming drop in a liquid–liquid system. Exp Fluids 44(4):565–575. doi:10.1007/s00348-007-0416-x

Tretheway DC, Meinhart CD (2002) Apparent fluid slip at hydrophobic microchannel walls. Phys Fluids 14(3):L9–L12

Tretheway DC, Meinhart CD (2004) A generating mechanism for apparent fluid slip in hydrophobic microchannels. Phys Fluids 16(5):1509–1515

van der Graaf S, Steegmans MLJ, van der Sman RGM, Schroen CGPH, Boom RM (2005) Droplet formation in a T-shaped microchannel junction: a model system for membrane emulsification. Colloids Surf Physicochem Eng Aspects 266(1–3):106–116

Wereley ST, Gui L, Meinhart CD (2002) Advanced algorithms for microscale particle image velocimetry. Aiaa J 40(6):1047–1055

Williams SJ, Park C, Wereley ST (2010) Advances and applications on microfluidic velocimetry techniques. Microfluid Nanofluid 8(6):709–726. doi:10.1007/s10404-010-0588-1

Woerner M (2012) Numerical modeling of multiphase flows in microfluidics and micro process engineering: a review of methods and applications. Microfluid Nanofluid 12(6):841–886. doi:10.1007/s10404-012-0940-8

Yeo LY, Chang H-C, Chan PPY, Friend JR (2011) Microfluidic devices for bioapplications. Small 7(1):12–48. doi:10.1002/smll.201000946